applied sciences

MDPI

Article

Time-Synchronized Microwave Cavity Resonance Spectroscopy and Laser Light Extinction Measurements as a Diagnostic for Dust Particle Size and Dust Density in a Low-Pressure Radio-Frequency Driven Nanodusty Plasma

Tim Donders *, Tim Staps and Job Beckers

Department of Applied Physics, Eindhoven University of Technology, P.O. Box 513, 5600 MB Eindhoven, The Netherlands
* Correspondence: t.j.m.donders@tue.nl

Abstract: In a typical laboratory nanodusty plasma, nanometer-sized solid dust particles can be generated from the polymerization of reactive plasma species. The interplay between the plasma and the dust gives rise to behavior that is vastly different from that of pristine plasmas. Two of the key parameters in nanodusty plasma physics are, among other things, the dust particle size and the dust density. In this work, we introduce a novel method for the determination of these two quantities from the measurement of the free electron density using microwave cavity resonance spectroscopy and laser light extinction measurements. When comparing these two measurements to theory, one can determine the best-fitting dust particle size and dust density. Generally, cyclic behavior of the dust particle size and dust density was observed, of which the trends were relatively insensitive to varying the most stringent input assumptions. Finally, this method has been used to explore the behavior of the dust particle size and dust density for varying plasma powers.

Keywords: nanodusty plasma; low-pressure dusty plasma; dust growth; dust particle size; dust density; nanoparticle

Citation: Donders, T.; Staps, T.; Beckers, J. Time-Synchronized Microwave Cavity Resonance Spectroscopy and Laser Light Extinction Measurements as a Diagnostic for Dust Particle Size and Dust Density in a Low-Pressure Radio-Frequency Driven Nanodusty Plasma. *Appl. Sci.* **2022**, *12*, 12013. https://doi.org/10.3390/app122312013

Academic Editor: Dawei Liu

Received: 20 October 2022
Accepted: 22 November 2022
Published: 24 November 2022

1. Introduction

A dusty plasma comprises a partially ionized gaseous medium containing electrically charged solid dust particles, of which the size can typically range between a few nanometers and several micrometers [1,2]. Typical examples of dusty plasmas can be found both in astrophysics [3,4] and in industrial applications [5]. In the field of astrophysics, one can find dusty plasmas in the rings of Saturn [6–8], around Jupiter [9,10], and in the form of accretion disks [11]. In industrial applications, dust particles in plasma applications are often seen as a form of contamination [12]. For example, in photolithography machines, the presence of small dust particles in vulnerable places in the machine can lead to a drastic decrease in the microchip quality [13]. Therefore, the physics behind the release of (nano) particles from surfaces is a widely researched topic [14,15].

These applications formed the spark for investigating dusty plasmas in laboratory environments [1,16]. As dust particles in a plasma behave as electrostatically floating bodies, they will attain charge from the plasma. Generally, dust particles tend to charge negatively since the electron mobility is much higher than the ion mobility [2], which implies that the electron current towards the particle initially outweighs the ion current until an equilibrium between these currents is reached for a certain negative particle surface potential. This interplay between the dust particles and the plasma gives rise to a broad range of physical phenomena; strongly coupled (plasma-dust and dust-dust) interactions manifest in the form of crystallization [17], phase transitions [18], chain formation [19,20], or self-excited dust density waves [21–26]. In all of these phenomena, the dust charge plays a major role.

The charge of micrometer sized dust particles has been measured using particle resonance methods [27,28] or by applying external electric fields [29,30]. For nanodusty plasmas, the dust charge density can for instance be estimated using laser-induced photodetachment (LIP) [31].

Apart from the charge, the dust particle size is a relevant parameter, especially in the case of nanodusty plasmas. In this type of dusty plasmas, dust particles are chemically grown in the plasma by means of admixing a reactive precursor gas with a noble background gas. For this, organic precursors (such as acetylene (C_2H_2) [32] or methane (CH_4) [33,34]), silicon-based [35], or organosilicon precursor gases [36,37] are often used. Such precursor gases easily dissociate into fragments, after which these fragments efficiently polymerize into larger species. In a nanodusty plasma, generally the growth can qualitatively be described in three distinct phases [38,39]. During the (i) nucleation phase, the plasma chemistry dictates the growth of protoparticles of only a few nanometers in size, which can be charged either positively, negatively, or neutrally. Once a critical density of protoparticles has been reached, the (ii) coagulation phase begins, during which the particles will rapidly coalesce. This phase is suddenly terminated by Coulombic repulsion, as the particles attain a permanently negative charge with increasing size [38,40]. From this point on, dust particle growth happens by means of (iii) accretion or surface growth, which is characterized by the collection of positive ions and radicals from the plasma. As the dust particles grow in size, the magnitude of the (outward pointing) ion drag force increases faster than the (inward pointing) electrostatic force, which causes the growing dust particles to drift outwards. Once the center of the discharge is sufficiently dust-free, a subsequent growth cycle can start.

In the field, much work has been devoted to modeling, ranging from detailed chemistries [41–45] to (discrete) sectional models for particle growth [46–48]. From an experimental point of view, several optical diagnostic techniques have been developed for monitoring the dust particle size, such as Mie ellipsometry [49–54], light extinction spectroscopy (LES) [55,56], time-resolved laser-induced incandescence (TIRE-LII) [57–61], and laser-induced particle explosive evaporation (LIPEE) [62,63].

In this work, we introduce a new method for in situ particle sizing, based on time-synchronized measurements of the free electron density in the plasma and laser light extinction by the dust cloud confined in it. Using these two quantities allows resolving both the dust particle size and the dust density. The experimental implementation of this method is relatively straightforward and, more importantly, the measurements are non-intrusive.

This work can be seen as a follow-up after our previous work [36]. The basis of the experimental setup and the primary data set is the same, but the focus is on the development of the fitting method. The newly developed method proves to expand the understanding of the measurements, which supports the choice of using the same data set for a direct comparison between the results. The structure of this work is as follows: In Section 2 the experimental setup for the measurement of the free electron density and the laser light extinction is explained in more detail. Section 3 continues by explaining how these types of measurements can be used to disambiguate the dust particle size and the dust density. Section 4 shows the typical results of these measurements and Section 5 summarizes the most important findings of this work.

2. Experiment

This section will describe the used experimental setup. Section 2.1 shows a general description of the equipment needed for plasma generation and gas handling. The section will continue with the discussion of the two key diagnostics for the developed fitting method: (i) microwave cavity resonance spectroscopy (discussed in Section 2.2) and (ii) laser light extinction (discussed in Section 2.3).

2.1. Gas Handling and Plasma Generation

Figure 1 shows a schematic top view of the used experimental setup. Inside a vacuum vessel, a plasma was generated inside a stainless steel cylindrical cavity with an inner radius of $R = 0.033\,\mathrm{m}$ and a height of $H = 0.04\,\mathrm{m}$. The base pressure of the setup was $1 \times 10^{-5}\,\mathrm{Pa}$. In the experiments, argon was used as a background gas and hexamethyldisiloxane (HMDSO, $(CH_3)_3{-}Si{-}O{-}Si{-}(CH_3)_3$) was used as a reactive precursor gas, with partial pressures of $p_{Ar} = 5.7\,\mathrm{Pa}$ and $p_{HMDSO} = 0.8\,\mathrm{Pa}$, respectively. This leads to an HMDSO content of 12.3% and a total pressure of $p = 6.5\,\mathrm{Pa}$. The plasma was generated using a sinusoidal voltage with a frequency of $f = 13.56\,\mathrm{MHz}$ applied to the top wall of the cavity, while the side and bottom are electrically grounded. During the experiments, the plasma power was measured to be $P = 23\,\mathrm{W}$ using an impedance meter (Impedans Octiv Poly).

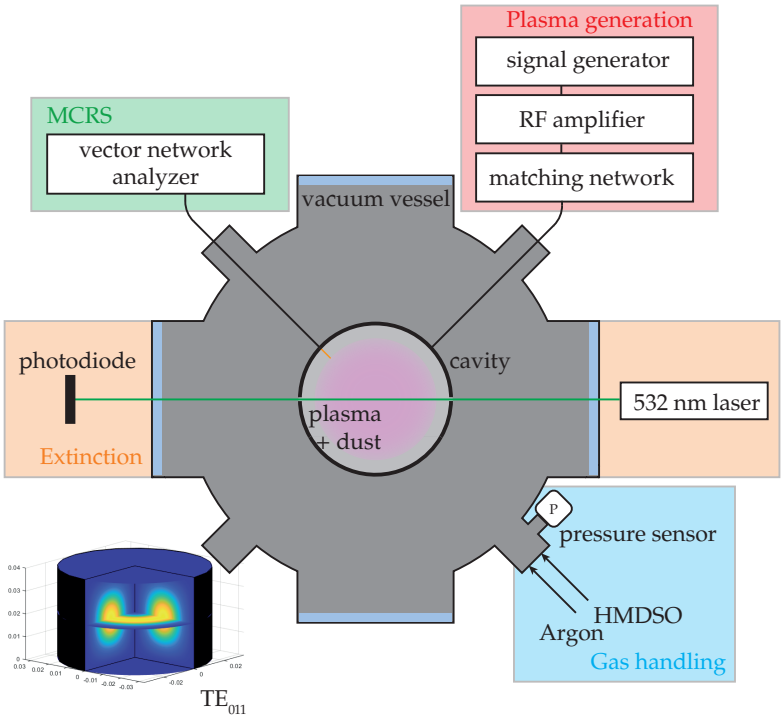

Figure 1. Schematic top view of the experimental setup for monitoring dust particle growth in a low-pressure Ar-HMDSO plasma. The plasma was generated in a cylindrical cavity inside a vacuum vessel. The free electron density of the plasma was measured using a vector network analyzer. The TE_{011} mode was used for the MCRS measurements, of which the mode pattern is shown in the inset. Simultaneously, a green laser ($\lambda = 532\,\mathrm{nm}$) was used to perform laser light extinction measurements on the dust cloud.

2.2. Microwave Cavity Resonance Spectroscopy

The first main diagnostic of this work is microwave cavity resonance spectroscopy (MCRS), which was used to experimentally measure the free electron density in the plasma. This diagnostic technique is based on the determination of the shift in resonance frequency of a standing microwave mode in a cavity due to a change in the permittivity of the medium through which the microwaves propagate. In the past, this measurement has been used to measure the free electron density in a wide variety of plasma types [31,64–66]. The difference between the resonance frequency with plasma present f_p and the vacuum resonance frequency f_1 is therefore a direct measure of the volume-averaged free electron density $\hat{n}_e$. In the current set of experiments, microwaves were introduced using a vector network analyzer (VNA, Keysight E5072A) in the frequency range f = 5.0–5.2 GHz, closely around the resonance frequency of the TE_{011} mode in the cavity in vacuum (i.e., without plasma), which was determined to be $f_1 = 5.099\,\mathrm{GHz} \pm 0.150\,\mathrm{MHz}$. This mode was chosen

since its mode pattern (a toroidal region with a maximum intensity at $r = R/2$, see the inset in Figure 1) best resembles the region where the dust particles are expected to be present. The amount of input microwave power into the cavity was fixed at $P_{\text{microwave}} = 1\,\text{mW}$, whereas the amount of reflected power was monitored at a sample rate of 10 Hz for the full frequency range. It can be noted that the microwave power is much less than the plasma power, which indicates that the measurements are non-invasive. This resulted in a reflected power spectrum as a function of the microwave frequency f, which represented an (inverted) Lorentzian-type of power response $P(f)$, of which the frequency corresponding to the minimum in reflected power reveals the resonance frequency at the moment of measurement. The resonance frequency was determined using a Matlab program that fitted the Lorentzian curve to the measured reflected power spectra. In this way, the shift in resonance frequency $\Delta f = f_\text{p} - f_1$ has been determined over the course of the evolution of the dusty plasma.

The Slater perturbation theorem relates the shift in resonance frequency Δf to the change in permittivity, from which the volume-averaged free electron density $\hat{n}_\text{e}$ in the plasma can be derived as [67]:

$$\hat{n}_\text{e} = \frac{8\pi^2 \varepsilon_0 m_\text{e} f_\text{p}^2}{e^2 f_1} \frac{\Delta f}{\mathcal{V}}, \tag{1}$$

with the vacuum permittivity denoted by ε_0, the plasma frequency by f_p, the elementary charge by e, the vacuum resonance frequency by f_1 (i.e., without plasma), and the electric-field-squared-weighted volume ratio by $\mathcal{V}$. The fact that the plasma volume V_p does not occupy the complete cavity volume V_c (due to the sheath regions at the plasma boundary) is accounted for by this electric-field-squared-weighted volume ratio $\mathcal{V}$:

$$\mathcal{V} = \frac{\iiint_{V_\text{p}} |\mathbf{E}(\mathbf{r})|^2 d^3\mathbf{r}}{\iiint_{V_\text{c}} |\mathbf{E}(\mathbf{r})|^2 d^3\mathbf{r}}. \tag{2}$$

The microwave electric field $\mathbf{E}(\mathbf{r})$ is determined using COMSOL Multiphysics using the dimensions of the cavity used in the experiments, and zero potential boundary conditions at the walls of the cavity.

2.3. Laser Light Extinction

The second key diagnostic for this approach is laser light extinction. The experimental implementation is rather straightforward: A green laser ($\lambda = 532\,\text{nm}$) was sent radially through the center of the cavity via two slits. After passing through the cavity, its intensity was measured using a photodiode (Thorlabs DET10A). When a dust cloud is present in the cavity, part of the light will be scattered or absorbed by the dust particles, which decreases the intensity measured by the photodiode. The quantity of interest is the transmittance $\hat{T}$:

$$\hat{T} = \frac{I}{I_0}, \tag{3}$$

i.e., the ratio between the light intensity with (I) and without (I_0) the presence of a dust cloud, respectively. The transmittance of the dust cloud was recorded as a function of time using an oscilloscope (Agilent DSO7054A).

3. Methods

The time-synchronized measurement of the free electron density in the plasma and laser light extinction by the dust cloud can be used to determine the dust particle size and dust density. Figure 2 provides a schematic overview of the fitting method, which will be discussed in more detail in the remainder of this section. In Section 3.1, the experimental part (depicted in green in Figure 2) is discussed: The raw data is shown and the measured quantities are derived. Section 3.2 follows by deriving the matching quantities from

theory (depicted in blue in Figure 2). Section 3.3 continues with the fitting procedure for obtaining the dust particle size and density from the decrease in electron density and the transmittance, as shown by the central part in Figure 2.

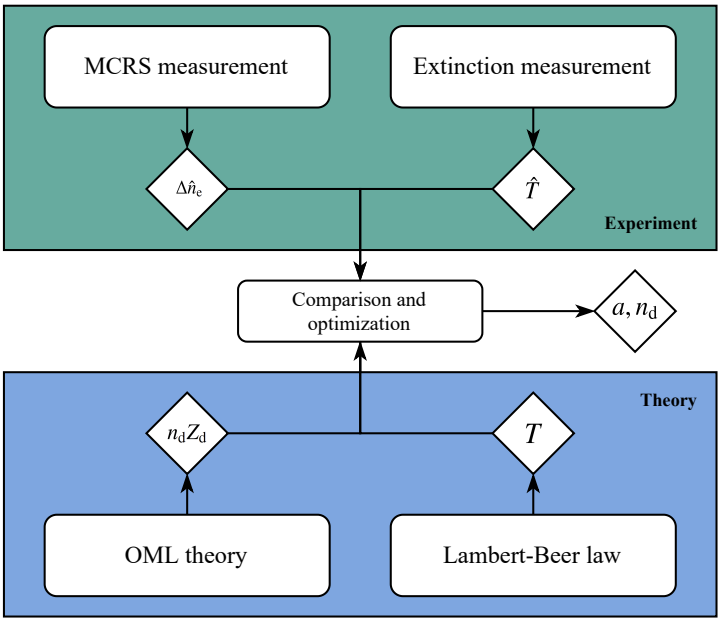

Figure 2. Flowchart for the retrieval of the best fitting dust particle size and dust density from the comparison of experimental MCRS and extinction measurements and the OML theory and the Lambert-Beer law.

3.1. Measurement Data

Figure 3 shows the experimental measurement data, i.e., the free electron density $\hat{n}_e$ measured using MCRS in panel (a) and the transmittance signal $\hat{T}$ measured by laser light extinction in panel (b), from the moment of plasma ignition at $t = 0\,\mathrm{s}$ until the end of the second dust growth cycle at $t = 250\,\mathrm{s}$. In this section, we will discuss the general behavior of the signals over the course of time.

From the free electron density, it can be seen that the electron density is initially about $\hat{n}_e \approx 12 \times 10^{15}\,\mathrm{m}^{-3}$, but quickly decreases by a factor of 6 to $\hat{n}_e \approx 2 \times 10^{15}\,\mathrm{m}^{-3}$ about 20 s after plasma ignition. For the current method, we are mainly interested in the decrease of the electron density with respect to the initial value, $\Delta\hat{n}_e(t) = \hat{n}_{e,\mathrm{initial}} - \hat{n}_e(t)$ (see Figure 3a), since it can be attributed to the charging of the growing dust particles. Note that here the subscript 'initial' refers to the moment shortly after ignition of the plasma; i.e., when the electron and ion densities have built up, but when there are no dust particles yet. In practice, this corresponds to the values at the time of the first measurement point, which is typically measured 100 ms after switching on the plasma. At about $t = 35\,\mathrm{s}$ the transmittance starts to decay linearly. During this period, the electron density changes only slightly up to the point that the transmittance value is at its minimum. This moment in time, corresponding to a minimum in $\hat{T}$, represents the formation of the void: a volume in the discharge center from which the dust grains are being removed when the outward-pointing ion drag force overcomes the inward-pointing electrostatic force. After this moment, both the electron density and transmittance start to increase again, signaling that the dust grains are effectively being transported toward the plasma edge and will eventually leave the plasma. It is interesting to note that both the electron density (around $t = 110\,\mathrm{s}$) and the transmittance (around $t = 150\,\mathrm{s}$) do not fully recover back to their initial values before the subsequent growth cycle starts. This indicates that a new growth cycle commences as soon as the center of the discharge is sufficiently dust-free, even though there is still a substantial amount of dust in the periphery.

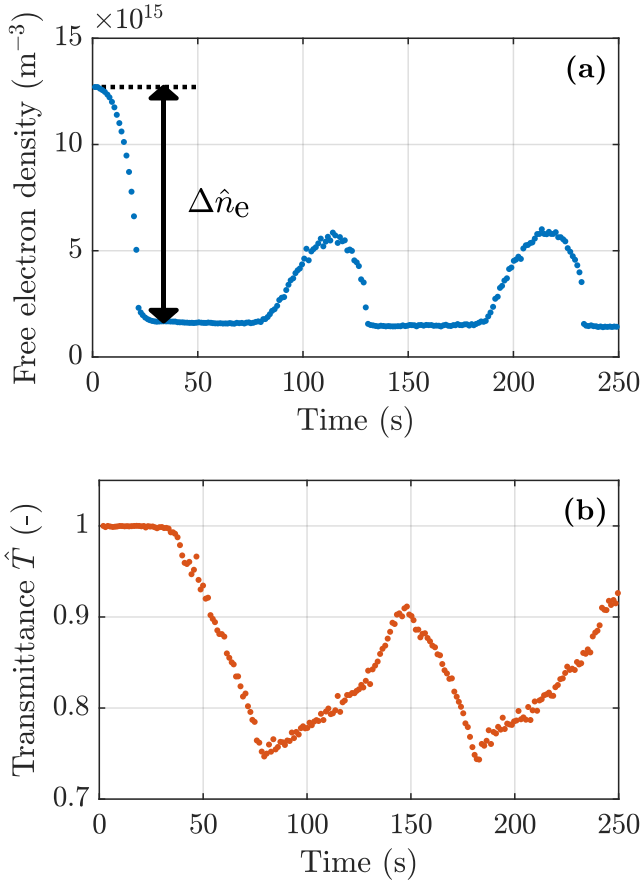

Figure 3. The free electron density $\hat{n}_e$ in panel (**a**) and the transmittance $\hat{T}$ signal in panel (**b**) from the moment of plasma ignition until the end of the second growth cycle. (**a**) The free electron density has been obtained using microwave cavity resonance spectroscopy (MCRS), which clearly shows a repetitive growth pattern after the initial cycle. (**b**) The transmittance signal shows similar repetitive features, but also sharp minima and maxima that are indicative of additional growth features. The data in this Figure has been published in Tim Jacobus Maria Donders et al. [36] 2022 J. Phys. D: Appl. Phys. 55 395203 (https://doi.org/10.1088/1361-6463/ac802a) licensed under a Creative Commons Attribution (CC BY) license and used with the permission of the authors.

3.2. Theory

3.2.1. Microwave Cavity Resonance Spectroscopy

The quasi-neutrality condition in the plasma bulk is used to relate the change of the free electron density to the dust charge density, i.e., the total amount of charge captured by the dust grains. The quasi-neutrality condition states that the total amount of positive charge should be balanced by the total amount of negative charge, as:

$$n_{i+} = n_e + n_{i-} + n_d|Z_d|, \tag{4}$$

where n_{i+} and n_{i-} represent the positive and negative ion density, respectively, n_d the dust density, and Z_d the amount of elementary charges on the dust grains. Here, it is assumed that the ion densities do not change during the experiment so that $n_{i+}(t) = n_{i+,\text{initial}}$ and $n_{i-}(t) = n_{i-,\text{initial}}$, and that $n_{d,\text{initial}} = 0$ as dust grains are not formed yet. Using these assumptions, the change of electron density Δn_e can be derived from Equation (4):

$$\begin{aligned} \Delta n_e(t) &= n_{e,\text{initial}} - n_e(t) \\ &= (n_{i+,\text{initial}} - n_{i-,\text{initial}}) - (n_{i+}(t) - n_{i-}(t) - n_d(t)Z_d(t)) \\ &= n_d(t)Z_d(t). \end{aligned} \tag{5}$$

The equilibrium charge number Z_d of dust particles with a radius a is governed by the balance of currents towards a dust grain:

$$I_{i+} = I_{i-} + I_e, \tag{6}$$

where the positive ion current I_i (i.e., attracted towards the particle) is defined as:

$$I_{i+} = e\pi a^2 n_i \sqrt{\frac{8k_B T_i}{\pi m_i}} \left(1 - \frac{eV_d}{k_B T_i}\right). \tag{7}$$

For electrons and negative ions (i.e., repelled from the particle), the current is defined as

$$I_{e,i-} = -e\pi a^2 n_{e,i-} \sqrt{\frac{8k_B T_{e,i-}}{\pi m_{e,i-}}} \exp\left(\frac{eV_d}{k_B T_{e,i-}}\right), \tag{8}$$

based on the orbital-motion-limited (OML) theory [68]. Taking a closer look at the OML expressions, it can be seen that the negative ion current is insignificant with respect to the electron current by evaluating the ratio between the currents:

$$\begin{aligned} \frac{I_{i-}}{I_e} &= \frac{-e\pi a^2 n_{i-} \sqrt{\frac{8k_B T_{i-}}{\pi m_{i-}}} \exp\left(\frac{eV_d}{k_B T_{i-}}\right)}{-e\pi a^2 n_e \sqrt{\frac{8k_B T_e}{\pi m_e}} \exp\left(\frac{eV_d}{k_B T_e}\right)} \\ &= \frac{n_{i-}}{n_e} \frac{m_e T_{i-}}{m_{i-} T_e} \exp\left(\frac{eV_d}{k_B T_{i-}}\right) \ll 1, \end{aligned} \tag{9}$$

where typically $m_e \ll m_{i-}$, $T_{i-} \ll T_e$, and $\exp\left(\frac{eV_d}{k_B T_{i-}}\right) \ll 1$ because $eV_d \sim 1\,\text{eV}$ and $k_B T_{i-} \approx 0.026\,\text{eV}$ (at room temperature). As a consequence, the dust floating potential V_d can be determined from Equation (6) in combination with Equations (7) and (8), neglecting the contribution of I_{i-}. This relates to the equilibrium charge $Q_d = eZ_d$ following the spherical capacitor model:

$$Q_d = eZ_d = 4\pi\varepsilon_0 a V_d. \tag{10}$$

From Equation (5), it can be seen that the quantity $n_d Z_d$ can be related to the change in the electron density due to the formation and growth of the dust particles. In order to make the OML equations only a function of a and n_d, one should make reasonable assumptions for the (negative) ion density and the electron temperature. From modeling efforts in the nucleation phase of nanodusty plasmas [69,69–71], the (total) positive ion density is expected to be (usually about one order of magnitude) higher than the electron density, due to the presence of negative ions. Therefore, in this work it is assumed that at plasma ignition the total positive ion density is five-fold the electron density, i.e., $n_{i+,\text{initial}} = 5n_{e,\text{initial}}$, so that, by quasi-neutrality and the initial absence of dust, $n_{i-,\text{initial}} = 4n_{e,\text{initial}}$ and $n_{d,\text{initial}} = 0$. For the electron temperature a constant value of $T_e = 3\,\text{eV}$ is assumed. Section 4.2 provides more details about these assumptions and performs a sensitivity analysis.

3.2.2. Laser Light Extinction

Using the Lambert–Beer law [1], the transmittance can be related to properties of the dust particles:

$$T = \exp\left(-Q_{ext}(n, \lambda_{exc}, a)\pi a^2 n_d L\right). \tag{11}$$

In this equation, $Q_{ext}(n, \lambda_{exc}, a)$ is the extinction coefficient, a is the radius of the dust, n_d is the dust density, and L is the extinction path length, which is taken to be equal to the internal diameter of the cavity, i.e., $L = 2R = 0.066\,\text{m}$. The extinction coefficient is determined using Mie theory and is a function of the complex refractive index, the excitation wavelength, and the dust particle radius. Here, the refractive index at $\lambda_{exc} = 532\,\text{nm}$ of $n = 1.45 + 0.00i$ was used, as determined from spectroscopic ellipsometry measurements

on HMDSO thin films reported in literature [72]. Unfortunately, the optical characterization data of dust particles formed in a low-pressure Ar-HMDSO plasma is not available in current literature. It should therefore be noted that the processing conditions (i.e., pressure, power, and background gas) of the thin films are slightly different from the conditions in this work and that it is assumed that the optical properties of thin films are similar to those of a cloud of dust particles.

3.3. Optimization Procedure

This section will provide more details about the optimization procedure for obtaining the dust particle size and dust density from the measurements. As illustrated in Figure 2 and the previous sections, we have obtained two measured quantities $\left(\Delta\hat{n}_e, \hat{T}\right)$, which can be directly compared to theoretically determined values $(n_d Z_d, T)$ using Equations (5) and (11), respectively. For the sake of clarity, the experimentally measured quantities are denoted with a hat symbol, while the quantities derived from theory are not.

The optimization procedure works as follows: (i) For a wide range of a and n_d, the theoretical values of $(n_d Z_d, T)$ are calculated. Then, (ii) the relative errors with respect to the measured values $\left(\Delta\hat{n}_e, \hat{T}\right)$ are calculated using $\chi_{mcrs} = \left|\frac{n_d Z_d - \Delta\hat{n}_e}{\Delta\hat{n}_e}\right|$ and $\chi_{ext} = \left|\frac{T-\hat{T}}{\hat{T}}\right|$. Figure 4 shows a qualitative visualization of the relative errors for a single data point in the measured time trace. The red curve in the plot represents pairs of (a, n_d) for which the goodness of fit with respect to the MCRS measurements is high, i.e., the relative MCRS error χ_{mcrs} is low. The blue curve corresponds to a region for which the goodness of fit with respect to the extinction measurements is high, i.e., the relative extinction error χ_{ext} is low. Since both of the diagnostics are measured in a time-synchronized fashion and therefore probe the same sample of dust, the most probable (a, n_d) pair lies on the intersection of the two regions; where both χ_{mcrs} and χ_{ext} are low, which is indicated with the magenta region in Figure 4. In the example of Figure 4, this would result in a dust particle radius of $a = 110\,\text{nm}$ and a dust density of $n_d = 1.19 \times 10^{14}\,\text{m}^{-3}$, as indicated by the black circle.

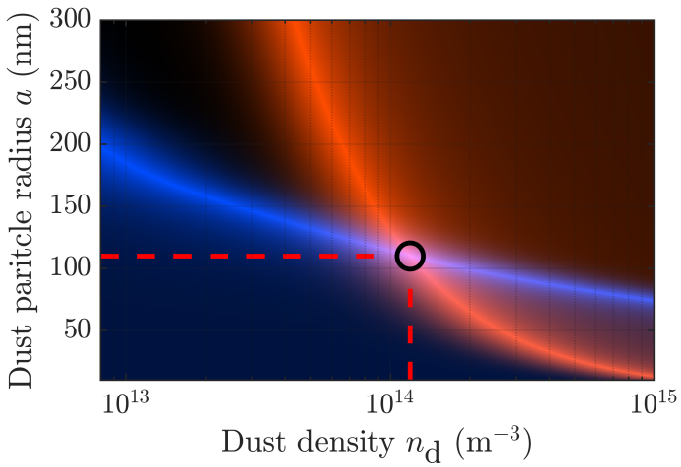

Figure 4. Visualization of the optimization procedure for a specific moment in time. The red region indicates pairs of a and n_d with a high goodness of fit with respect to the MCRS measurements (i.e., low relative MCRS error χ_{mcrs}), whereas the blue region indicates a high goodness of fit with respect to the extinction measurements (i.e., low relative extinction error χ_{ext}). Since the measurements are obtained in a time-synchronized way, the intersection of two regions (indicated in magenta) indicates the most likely (a, n_d) pair, here indicated by the black circle. In this case, the determined dust particle size and dust density are $a = 110\,\text{nm}$ and $n_d = 1.19 \times 10^{14}\,\text{m}^{-3}$, respectively.

4. Results and Discussion

This section shows the typical results of the determination of the dust particle size and density from combined MCRS and extinction measurements. Section 4.1 shows the general results of a measurement and compares the findings to similar works. Section 4.2 continues

with a sensitivity analysis for two quantities for which an assumption is necessary for the analysis and which are challenging to measure, namely the electron temperature and the negative ion density. Finally, in Section 4.3 the method is used to observe trends in the dust particle size and dust density when varying the plasma power.

4.1. General Results

In this section, the results of a typical time-resolved measurement of the dust particle size and dust density using the method proposed in this work are discussed. Using the developed optimization procedure explained in Section 3.3, the fitted dust particle radius a and the dust density n_d are shown in Figure 5. After igniting the plasma at $t = 0\,\mathrm{s}$, the dust particles will be generated through the polymerization of precursor species. The lower detection limit of the method is determined by the sensitivity of the extinction measurement; at early times, the dust particle size and/or density is too small to cause sufficient extinction of the laser light (i.e., $\hat{T} \approx 1$). Therefore, the fitting procedure is started when $\hat{T} \leq 0.99$, i.e., from $t = 34\,\mathrm{s}$ onward, resulting in a detection limit for particles with a radius of $a_\mathrm{min} = 59\,\mathrm{nm}$. As soon as the particles can generate enough extinction, a linear increase in the particle radius and a decrease in the dust density are observed. The growth rate in this linear regime is determined to be $1.30\,\mathrm{nm/s}$, which lies in the same range as the experiments performed in C_2H_2 reported elsewhere [50,73].

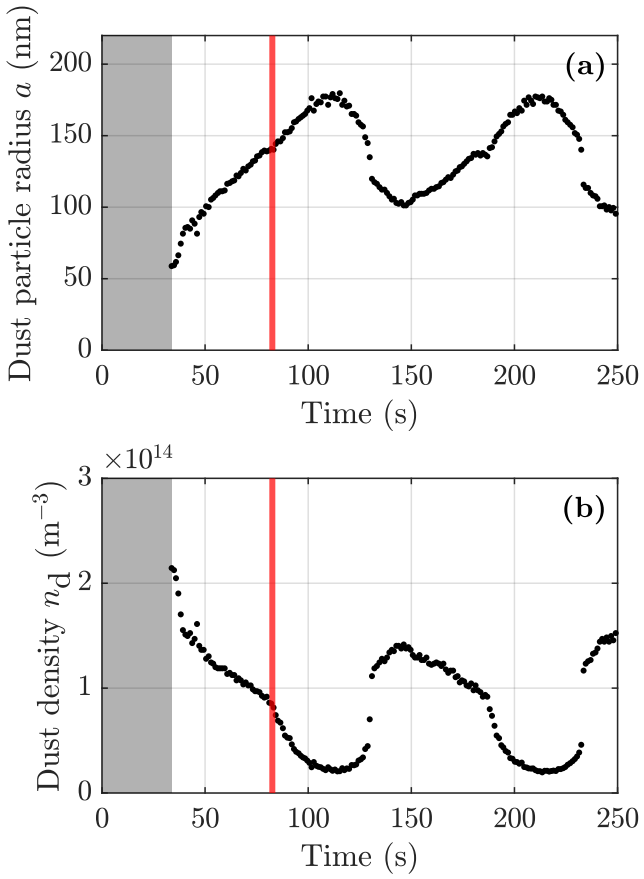

Figure 5. General result from the optimization procedure. The dust particle radius a is shown in panel (**a**) and the dust density n_d in panel (**b**). The gray-shaded area indicates the time period after discharge ignition during which the transmittance remains similar to a pristine plasma, which inhibits the proper determination of the dust particle size and density. The red lines mark the appearance of the void region, after which the path length L is no longer constant. A constant value of the electron temperature $T_\mathrm{e} = 3\,\mathrm{eV}$ and the negative ion density $n_{\mathrm{i}-} = 4n_\mathrm{e,initial}$ are assumed.

At around $t = 83\,\mathrm{s}$, the dust density transitions into a sharper decrease. This coincides with the turning point of the transmittance (see panel (b) in Figure 3 and is indicated with the red vertical lines in Figure 5), which signifies the appearance of the void. It should be noted that this implies that with the presence of the void the path length L (in Equation (11)) is overestimated, which eventually underestimates the quantity $a^2 n_\mathrm{d}$. From this moment on, the interpretation of the dust particle size and the dust density is complicated, since the path length is no longer fixed and since dust particles from two subsequent generations coexist, implying two different dust size distributions [51]. Therefore, the results shown in the following sections will be limited to the first growth cycle, and before the appearance of the void.

It is interesting to note that the mean dust charge Q_d also becomes available as soon as the dust particle radius and the dust density have been determined. Using Equations (5) and (10), the total (negative) dust particle charge is shown to become more negative over time, ranging from -50 elementary charges at $t = 34\,\mathrm{s}$ to -130 elementary charges at $t = 83\,\mathrm{s}$.

Several other researchers focused on the growth of dust particles in low-pressure nanodusty plasmas. In order to get a sense of whether the retrieved dust particle size is consistent with literature, an overview of the methods, precursor gases, and operating conditions have been provided in Table 1. The table indicates that under low-pressure conditions dust particles are produced with a typical radius of a = 100 nm to 300 nm, depending on the pressure, plasma power, and reactor geometry. Even though this range of dust particle sizes matches the retrieved particle size from the fitting procedure, a direct comparison is difficult. Therefore, in Appendix A.1, the method has been applied to MCRS and extinction data from previous work [31]. which could be directly compared to SEM images of the dust particles collected during the same measurement. In Appendix A, it is shown that the final retrieved particle size from the fitting method ($a_\mathrm{fit} = 156\,\mathrm{nm}$) is close to the mean dust particle size from the SEM image ($a_\mathrm{SEM,mean} = 146\,\mathrm{nm}$ and a standard deviation of $\sigma_\mathrm{SEM} = 7\,\mathrm{nm}$).

Table 1. Overview of the characteristics of low-pressure dust growth as reported in the literature.

Author	Used Method	Precursor	Plasma Power (W)	(Total) Pressure (Pa)	Growth Time (s)	Dust Particle Size (nm)
Groth et al. [50]	Ellipsometry	C_2H_2	8	24	85	200
Groth et al. [51]	Ellipsometry	C_2H_2	20	24	90	100
Dworschak et al. [73]	Ellipsometry + AFM	C_2H_2	8	25	130	150
Killer et al. [74]	Ellipsometry	C_2H_2	8	24	129	210
Tadsen et al. [23]	Ellipsometry	C_2H_2	8	11.5	85	184
Chutia et al. [75]	SEM	C_2H_2	1	20	600	300
Van de Wetering et al. [61]	LII	C_2H_2	7	10	[a]	100–165 [b]
Mitic et al. [76]	White light scattering	C_2H_2	0.3	20	150	260
Eom et al. [57]	TiRe-LII	SiH_4	5	2.7	1000	200

[a]: Continuous C_2H_2 flow, switched off after 35 min, [b]: Depending on the refractive index data set.

4.2. Sensitivity Analysis for the Electron Temperature and the Negative Ion Density

As mentioned in Section 3.2.1, the theoretical determination of the charge density $n_\mathrm{d} Z_\mathrm{d}$ and the transmittance T depends strongly on the assumed electron temperature through Equation (8) and the negative ion density through Equation (4). Both the electron temperature and negative ion density are difficult to determine experimentally or by modeling, and should therefore be assumed based on typical values found in the literature. In order to assess the sensitivity of the fitting procedure to these assumptions, the fitting procedure is also evaluated for different values for T_e and $n_{\mathrm{i}-}$.

Figure 6 shows the results of varying only the electron temperature T_e, while still using the same data set. The figure depicts the obtained dust particle radius and dust density as a function of time for $T_\mathrm{e} = 2\,\mathrm{eV}$, $T_\mathrm{e} = 3\,\mathrm{eV}$ and $T_\mathrm{e} = 4\,\mathrm{eV}$. Variations in the electron temperature lead to relatively small changes; the average dust particle size variation over the measured time range is $-7.0\,\mathrm{nm}$ and $+5.1\,\mathrm{nm}$, for $T_\mathrm{e} = 2\,\mathrm{eV}$ and $T_\mathrm{e} = 4\,\mathrm{eV}$, respectively,

both with respect to the base case of $T_e = 3\,\mathrm{eV}$. For the dust density, the average variation is found to be $+0.50 \times 10^{14}\,\mathrm{m}^{-3}$ and $-0.26 \times 10^{14}\,\mathrm{m}^{-3}$, with respect to the default case.

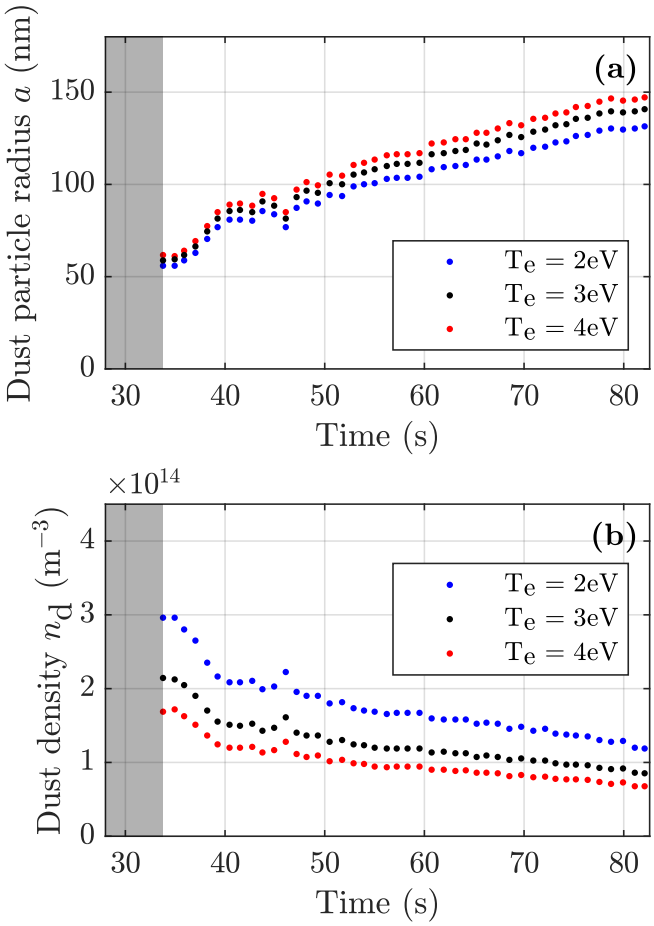

Figure 6. Sensitivity analysis for the electron temperature. Using the same raw data set, the dust particle radius (shown in panel (**a**)) and dust density (shown in panel (**b**)) are determined for an electron temperature ranging between T_e = 2–4 eV, while a constant value of the negative ion density $n_{i-} = 4n_{e,\mathrm{initial}}$ is assumed.

This dependency can be explained as follows: From the OML theory, it can be derived that the dust floating potential V_d increases with the increasing electron temperature T_e. Physically, this can be understood from the fact that a stronger potential barrier is necessary to repel more energetic electrons. For a constant or increasing a, the dust charge Z_d also increases with increasing T_e, which implies a larger Coulomb repulsion among the dust particles. Via Equation (5), it can be seen that n_d must decrease for a (fixed) measured $\Delta\hat{n}_e$. Using the Lambert–Beer law in Equation (11), it can be seen that the dust particle radius a indeed must increase with the decreasing dust density n_d for a fixed value of the measured transmittance.

Figure 7 shows the effect of varying the negative ion density n_{i-}. Here, we see the dust particle radius and dust density as a function of time for $n_{i-} = 2n_{e0}$, $n_{i-} = 4n_{e0}$ and $n_{i-} = 8n_{e0}$. The variations in dust particle radius are similar in magnitude to the deviations due to variations in the electron temperature; the average dust particle size variation over the measured time range is $+9.7\,\mathrm{nm}$ and $-11.4\,\mathrm{nm}$, for $n_{i-} = 2n_{e0}$ and $n_{i-} = 8n_{e0}$, respectively, both with respect to the default case of $n_{i-} = 4n_{e0}$. Similarly, the average difference in the dust density is about $-0.44 \times 10^{14}\,\mathrm{m}^{-3}$ and $+0.95 \times 10^{14}\,\mathrm{m}^{-3}$, compared to the default case.

These trends can be explained as follows: For a higher negative ion density, the positive ion density also increases, which follows from the quasi-neutrality condition shortly after igniting the plasma. An increase in the positive ion density n_{i+} results in a larger ion current, which allows a higher electron current at the floating potential, as Equation (6) suggests. This implies that the floating potential becomes less negative for increasing the negative ion density, and that the dust charge Z_d decreases for the fixed dust particle radius a. For a fixed $\Delta\hat{n}_e$, this results in a higher dust density n_d. From the Lambert–Beer law, it can be seen that this implies a lower dust particle radius a, which is consistent with the effect of a decreasing dust charge Z_d.

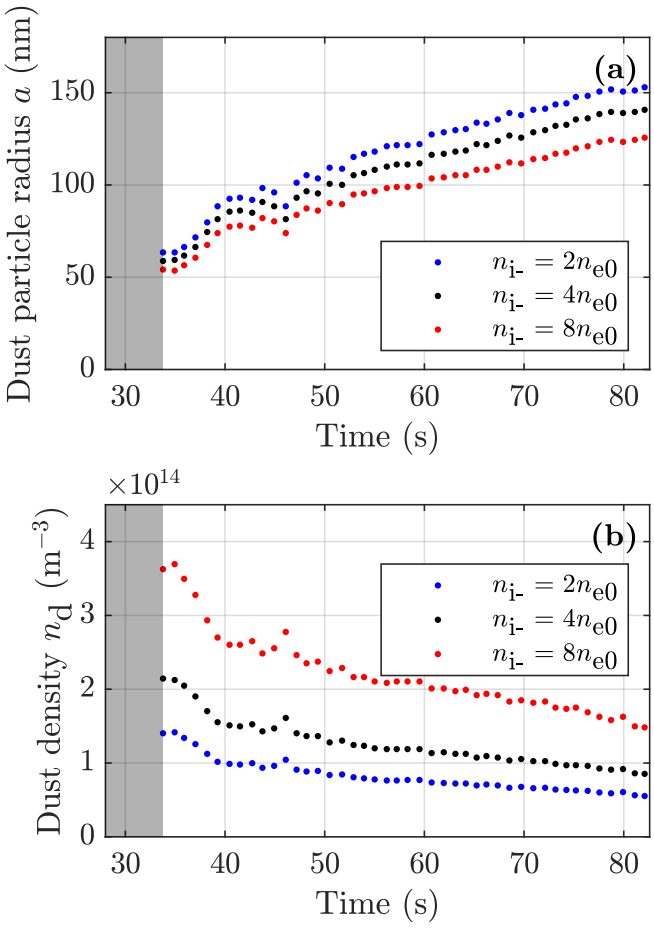

Figure 7. Sensitivity analysis for the negative ion density. Using the same raw data set, the dust particle radius (shown in panel (**a**)) and dust density (shown in panel (**b**)) are determined for negative ion densities ranging between $n_{i-} = 2$–$8n_{e,initial}$, while a constant value of the electron temperature $T_e = 3\,eV$ is assumed.

4.3. Influence of Changing Plasma Power on the Dust Particle Size and Dust Density

In the previous sections, we have introduced the method of determining the dust particle radius and the dust density from the measurement of the free electron density and the laser light extinction. In this section, we will continue by investigating the behavior of the dust particle radius and dust density as a function of plasma power. In these experiments, the partial pressures of argon and HMDSO are similar to those described in Section 3.1, while the power is varied from 8 W to 23 W. In line with the reasoning presented in Section 4.1 we selected the point in time right before the formation of the void, which coincides with the turning point in the transmittance (see Figure 3b). At this point, the dust particle radius and the dust density were recorded and plotted in Figure 8, both as a function of plasma power. In this Figure, the error bars arise from the propagation of

errors in the measured electron density $\hat{n}_e$ and the transmittance $\hat{T}$, which via the fitting procedure results in errors in the estimated a and n_d. In order to guide the eye, polynomial fits are included through the data points.

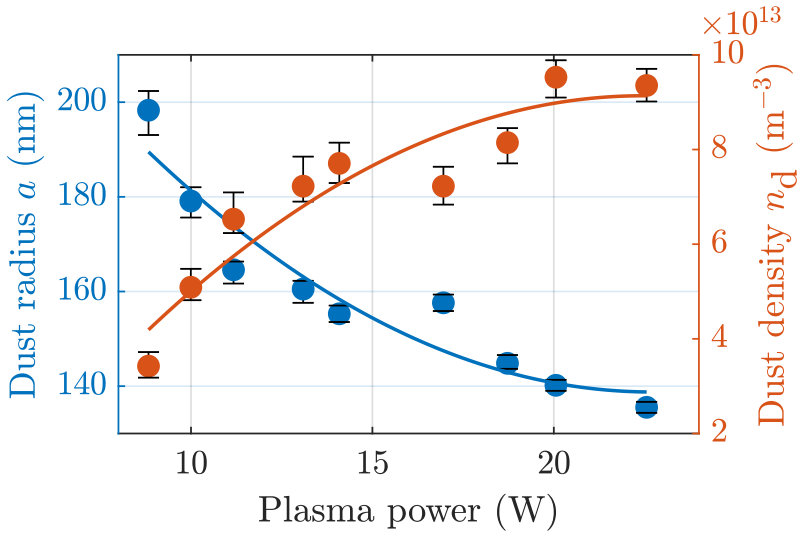

Figure 8. Overview of the results of the fitting procedure for the plasma power scan. The dust particle radius a (in blue circles) and the dust density n_d, both at the moment of formation of the void, are plotted as a function of plasma power. The error bars are the result of the errors in the measured electron density $\hat{n}_e$ and transmittance $\hat{T}$, as propagated through the fitting procedure. Again, a constant value of the electron temperature $T_e = 3\,\mathrm{eV}$ and the negative ion density $n_{i-} = 4n_{e,\mathrm{initial}}$ are assumed.

Figure 8 shows that by increasing the plasma power, the determined dust particle radius decreases while the dust density increases. By increasing the plasma power, (i) the overall plasma densities increase, while (ii) the growth cycle time decreases. For both effects, we will hypothesize about what happens to the resulting dust particle size a during the accretion phase. An increase in the plasma densities will increase the ion/radical fluxes towards the particle, leading to faster particle growth. The decreasing growth cycle time is a direct result of a change in the force balance acting on the particles. By increasing the plasma power, both the densities and the electric field strength increase, which eventually causes the ion drag force to be able to overcome the electrostatic force at shorter timescales [36]. This leads to a shorter growth cycle, which translates to a shorter residence time of the dust particles in the plasma and eventually leads to smaller dust particles.

From the previous discussion, the two mentioned effects counteract each other. In our previous work [36] it was argued that using the transmittance $\hat{T}$ enabled measuring only the combined quantity $a^2 n_d$, which made it difficult to differentiate between effects in the dust particle size and the dust density. However, using the newly developed method, Figure 8 shows that we are able to disentangle the behavior of the dust particle size and density evolution. This indicates that for higher plasma power, the effect of the shorter growth cycle leads to smaller dust particles, even though the fluxes towards the dust particles' surfaces are larger.

5. Conclusions

In this work, we introduced a novel method for determining the dust particle size and dust density in a low-pressure nanodusty Ar-HMDSO plasma, derived from measurements of the free electron density and laser light extinction. Comparing the measured values of the decrease of the electron density and the transmittance to those predicted by OML theory and the Lambert–Beer law, respectively, the combined error can be minimized such that the best-fitting values of the dust particle size and dust density can be determined.

As expected from the raw data and literature, the dust growth in the first growth cycle

is found to be linear, with a typical dust particle size of $\sim$140 nm right before the appearance of the void. The dust density is usually in the order of $\sim 10^{14}$ m^{-3}. Furthermore, it was observed that the interpretation of the data can become obscured by the appearance of the void region and the growth of a successive generation of dust particles. Generally, the dust particle size and dust density show opposite trends: When the dust particle size increases, the dust density decreases. The fitting procedure relies on assumptions of the electron temperature and the negative ion density; two quantities that are difficult to estimate or experimentally determine. The sensitivity of the fitting procedure to these parameters was investigated, which yielded similar trends in both dust particle size and density, while only the absolute values shifted. Finally, the method was used to investigate the dependence of the dust particle size and dust density on the plasma power. Interestingly, a lower plasma power yielded larger dust particle sizes, which is a direct consequence of the slower dust growth cycle, i.e., the longer residence time in the plasma.

The proposed fitting procedure shows that the time-synchronized measurement of the free electron density of the plasma and the laser light extinction by the dust cloud can reveal information about the dust particle size and dust density. This novel, experimentally convenient and non-intrusive method provides more insight into the fundamentals of nanodusty plasma physics.

Author Contributions: Conceptualization, J.B.; Data curation, T.D.; Formal analysis, T.D. and T.S.; Funding acquisition, J.B.; Investigation, T.D. and T.S.; Methodology, T.D.; Software, T.D.; Supervision, J.B.; Writing—Original draft, T.D. and T.S. All authors have read and agreed to the published version of the manuscript.

Funding: This work has been financed by the Dutch Research Council (NWO) of the Netherlands, proj. 17–24 Synoptics n. 2.

Institutional Review Board Statement: Not applicable.

Informed Consent Statement: Not applicable.

Data Availability Statement: The measurement data is available from the corresponding author upon reasonable request. The computer code used for the data analysis and interpretation is available from the corresponding author upon reasonable request.

Acknowledgments: The authors would like to thank A.B. Schrader and P. Sanders for their skillful technical support.

Conflicts of Interest: Author T.J.A. Staps was employed by Prodrive Technologies B.V. The other authors declare no competing interests.

Abbreviations

The following abbreviations are used in this manuscript:

HMDSO	Hexamethyldisiloxane
LES	Light Extinction Spectroscopy
LIP	Laser-induced Photodetachment
MCRS	Microwave Cavity Resonance Spectroscopy
OML	Orbital Motion Limited
SEM	Scanning Electron Microscope
TIRE-LII	Time-resolved Laser-induced Incandescence
VNA	Vector Network Analyzer

Appendix A

Appendix A.1. Comparison of the Retrieved Dust Particle Size to SEM Measurements

This section describes the results of an experiment in which dust particles are grown and collected on a substrate. Subsequently, the particles on the substrate have been analyzed using a scanning electron microscope (SEM). The main goal of this section is to compare the dust particle size retrieved from the fitting procedure with that measured by the SEM.

The plasma power was similar to the experiments described in the main text ($P = 20\,\mathrm{W}$), but the pressure and mixing ratio are slightly different: $p_{\mathrm{Ar}} = 5.4\,\mathrm{Pa}$ and $p_{\mathrm{HMDSO}} = 1.6\,\mathrm{Pa}$. After 60 s of dust growth, the HMDSO flow was terminated, the plasma was switched off and some of the dust particles were collected on the SEM substrate. Figure A1 shows an SEM micrograph with 15 dust particles, labeled and marked by red circles. Using an edge detection filter, the size of the particles is measured under the assumption that the particles are spherical. The results of the size determination of the individual particles are shown in Table A1, from which the average dust particle size over the sampled particles is found to be $a = 146.2 \pm 6.8\,\mathrm{nm}$.

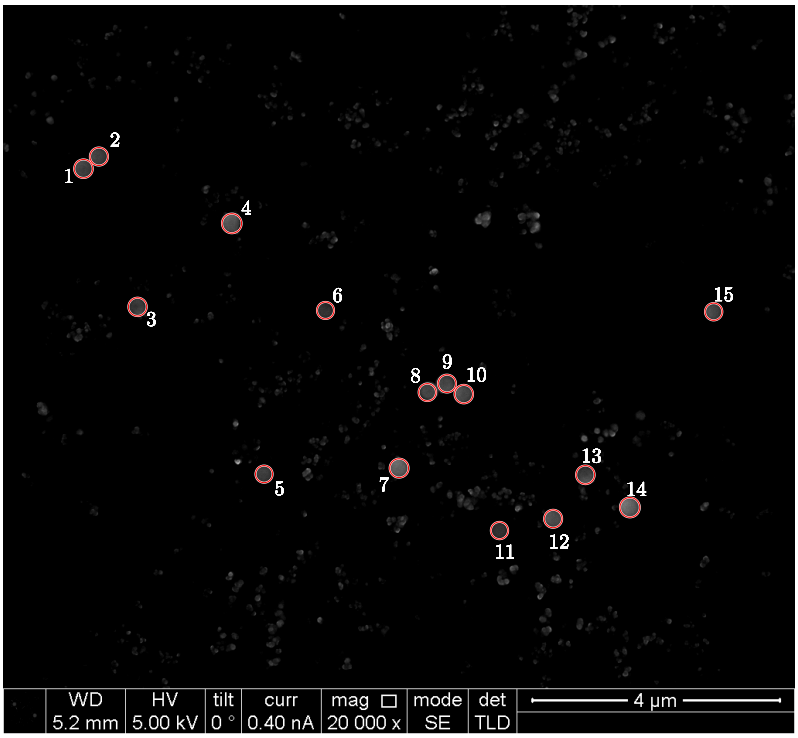

Figure A1. SEM micrograph of the dust particles collected after a growth period of $T = 60\,\mathrm{s}$. The individual particles are marked with a red circle and labeled. The scale bar on the bottom right indicates a size of 4 µm. The data in this figure has been published in Tim Jacobus Adrianus Staps et al. [31] 2022 J. Phys. D: Appl. Phys. 55 08LT01 (https://doi.org/10.1088/1361-6463/ac3581), licensed under a Creative Commons Attribution (CC BY) license and used with the permission of the authors.

Table A1. Calculated radii of the collected dust particles. The labels in this table coincide with the labels in Figure A1. From these 15 particles, the mean size and its standard deviation are calculated.

#	Radius (nm)	#	Radius (nm)	#	Radius (nm)
1	149.0	6	136.6	11	138.4
2	144.6	7	151.4	12	143.9
3	147.0	8	146.0	13	148.7
4	157.6	9	146.9	14	159.2
5	137.3	10	147.9	15	138.5
Total: $a = 146.2 \pm 6.8\,\mathrm{nm}$					

Similar to the results shown in Figure 5, the fitting procedure is started as soon as the transmittance took a value of $T \leq 0.99$. Figure A2 shows the results of the dust particle size inferred by the fitting procedure as a function of time. The red line indicates the mean of the dust particle size of the SEM image, with the 1σ and 2σ regions indicated by the red regions. At the time of switching off the plasma $t = 60\,\mathrm{s}$, the dust particle size is expected to be $a_{\mathrm{fit}} = 155.9\,\mathrm{nm}$, which is in the 2σ-region of the dust particle size determined

by the SEM image. Even though the difference between the measured and fitted dust particle size is quite small, several effects could explain the discrepancy. For example, the number of particles on the SEM image is relatively low and may therefore be an inaccurate measure of the dust particle size. On top of that, the dust particle size seems to be quite sensitive to the refractive index of the particles, via the extinction coefficient Q_{ext}. Since the refractive index data has been taken from a sample with different processing conditions, its value might explain the overestimation. Nevertheless, the fact that the dust particle sizes agree relatively well gives us some confidence in the developed fitting method and its underlying assumptions.

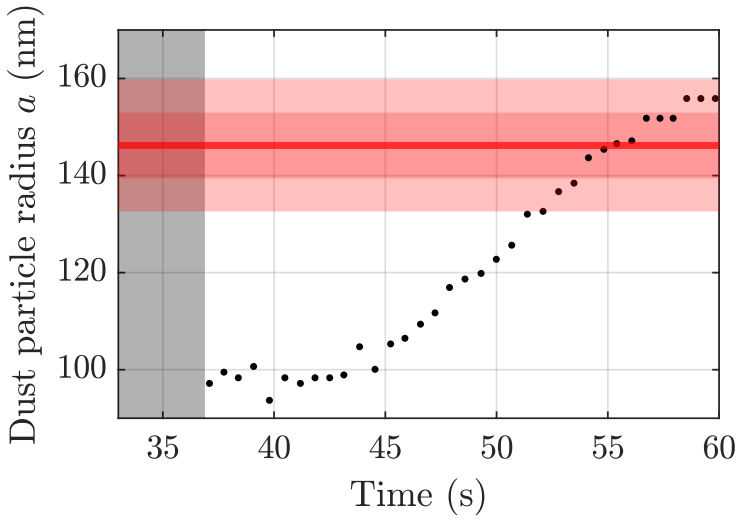

Figure A2. Result of the dust particle size for an experiment in which particles have been collected on an SEM substrate. The gray-shaded area indicates the time period after discharge ignition during which the transmittance remains similar to a pristine plasma, which inhibits proper determination of the dust particle size and density. The red line indicates the mean of the dust particle size inferred by the SEM image in Figure A1, while the dark and light red regions indicate the 1σ and 2σ regions, respectively. The raw data used for the fitting procedure and the production of this figure has been published in Tim Jacobus Adrianus Staps et al. [31] 2022 J. Phys. D: Appl. Phys. 55 08LT01 (https://doi.org/10.1088/1361-6463/ac3581), licensed under a Creative Commons Attribution (CC BY) license and used with the permission of the authors.

References

1. Melzer, A. *Physics of Dusty Plasmas-An Introduction*; Springer: Cham, Switzerland, 2019; Volume 962, p. 235. [CrossRef]
2. Piel, A. *Plasma Physics-An Introduction to Laboratory, Space and Fusion Plasmas*, 2nd ed.; Springer: Berlin/Heidelberg, Germany, 2017.
3. Bliokh, P.; Sinitsin, V.; Yaroshenko, V. *Dusty and Self-Gravitational Plasmas of Planetary Rings*; Springer, Dordrecht, The Netherlands, 1995; pp. 202–250. [CrossRef]
4. Horányi, M. Charged dust dynamics in the Solar System. *Annu. Rev. Astron. Astrophys.* **2003**, *34*, 383–418. [CrossRef]
5. Mendis, D.A. Progress in the study of dusty plasmas. *Plasma Sources Sci. Technol.* **2002**, *11*, A219. [CrossRef]
6. Wahlund, J.E.; André, M.; Eriksson, A.I.E.; Lundberg, M.; Morooka, M.W.; Shafiq, M.; Averkamp, T.F.; Gurnett, D.A.; Hospodarsky, G.B.; Kurth, W.S.; et al. Detection of dusty plasma near the E-ring of Saturn. *Planet. Space Sci.* **2009**, *57*, 1795–1806. [CrossRef]
7. Smith, B.A.; Soderblom, L.; Beebe, R.; Boyce, J.; Briggs, G.; Bunker, A.; Collins, S.A.; Hansen, C.J.; Johnson, T.V.; Mitchell, J.L.; et al. Encounter with Saturn: Voyager 1 Imaging Science Results. *Science* **1981**, *212*, 163–191. [CrossRef] [PubMed]
8. Smith, B.A.; Soderblom, L.; Batson, R.; Bridges, P.; Inge, J.; Masursky, H.; Shoemaker, E.; Beebe, R.; Boyce, J.; Briggs, G.; et al. A New Look at the Saturn System: The Voyager 2 Images. *Science* **1982**, *215*, 504–537. [CrossRef]
9. Krüger, H.; Bindschadler, D.; Dermott, S.F.; Graps, A.L.; Grün, E.; Gustafson, B.A.; Hamilton, D.P.; Hanner, M.S.; Horányi, M.; Kissel, J.; et al. Galileo dust data from the jovian system: 2000 to 2003. *Planet. Space Sci.* **2010**, *58*, 965–993. [CrossRef]
10. Krüger, H.; Linkert, G.; Linkert, D.; Moissl, R.; Grün, E. Galileo long-term dust monitoring in the jovian magnetosphere. *Planet. Space Sci.* **2005**, *53*, 1109–1120. [CrossRef]
11. Takeuchi, T.; Lin, D.N.C. Radial Flow of Dust Particles in Accretion Disks. *Astrophys. J.* **2002**, *581*, 1344–1355. [CrossRef]
12. Selwyn, G.S. Optical characterization of particle traps. *Plasma Sources Sci. Technol.* **1994**, *3*, 340–347. [CrossRef]

13. Scaccabarozzi, L.; Lammers, N.A.; Moors, R.; Banine, V. Particle Cleaning of EUV Reticles. *J. Adhes. Sci. Technol.* **2009**, *23*, 1603–1622. [CrossRef]
14. Van De Kerkhof, M.; Yakunin, A.M.; Kvon, V.; Nikipelov, A.; Astakhov, D.; Krainov, P.; Banine, V. EUV-induced hydrogen plasma and particle release. *Radiat. Eff. Defects Solids* **2022**, *2022*, 486–512. [CrossRef]
15. Van de Kerkhof, M.A.; Benschop, J.P.; Banine, V.Y. Lithography for now and the future. *Solid-State Electron.* **2019**, *155*, 20–26. [CrossRef]
16. Bonitz, M.; Horing, N.; Ludwig, P. *Introduction to Complex Plasmas*; Springer: Berlin/Heidelberg, Germany, 2010; Volume 59. [CrossRef]
17. Thomas, H.; Morfill, G.E.; Demmel, V.; Goree, J.; Feuerbacher, B.; Möhlmann, D. Plasma Crystal: Coulomb Crystallization in a Dusty Plasma. *Phys. Rev. Lett.* **1994**, *73*, 652. [CrossRef]
18. Vasilieva, E.V.; Petrov, O.F.; Vasiliev, M.M. Laser-induced melting of two-dimensional dusty plasma system in RF discharge. *Sci. Rep.* **2021**, *11*, 523. [CrossRef]
19. Hyde, T.W.; Kong, J.; Matthews, L.S. Helical structures in vertically aligned dust particle chains in a complex plasma. *Phys. Rev. E* **2013**, *87*, 53106. [CrossRef]
20. Melzer, A.; Buttenschön, B.; Miksch, T.; Passvogel, M.; Block, D.; Arp, O.; Piel, A. Finite dust clusters in dusty plasmas. *Plasma Phys. Control. Fusion* **2010**, *52*, 124028. [CrossRef]
21. Tadsen, B.; Greiner, F.; Groth, S.; Piel, A. Self-excited dust-acoustic waves in an electron-depleted nanodusty plasma. *Phys. Plasmas* **2015**, *22*, 113701. [CrossRef]
22. Tadsen, B.; Greiner, F.; Piel, A. Probing a dusty magnetized plasma with self-excited dust-density waves. *Phys. Rev. E* **2018**, *97*, 33203. [CrossRef]
23. Tadsen, B.; Greiner, F.; Piel, A. On the amplitude of dust-density waves in inhomogeneous dusty plasmas. *Phys. Plasmas* **2017**, *24*, 033704. [CrossRef]
24. Melzer, A.; Krüger, H.; Schütt, S.; Mulsow, M. Dust-density waves in radio-frequency discharges under magnetic fields. *Phys. Plasmas* **2020**, *27*, 33704. [CrossRef]
25. Killer, C.; Melzer, A. Global coherence of dust density waves. *Phys. Plasmas* **2014**, *21*, 63703. [CrossRef]
26. Chutia, B.; Deka, T.; Bailung, Y. Spatiotemporal evolution of a self-excited dust density wave in a nanodusty plasma under strong Havnes effect. *Phys. Plasmas* **2021**, *28*, 123702. [CrossRef]
27. Meijaard, P.; Staps, T.J.; Beckers, J. Step-wise excitation for the determination of the resonance frequency of a microparticle confined in a low pressure plasma. *Phys. Plasmas* **2021**, *28*, 083502. [CrossRef]
28. Carstensen, J.; Jung, H.; Greiner, F.; Piel, A. Mass changes of microparticles in a plasma observed by a phase-resolved resonance method. *Phys. Plasmas* **2011**, *18*, 033701. [CrossRef]
29. van Minderhout, B.; Peijnenburg, T.; Blom, P.; Vogels, J.; Kroesen, G.; Beckers, J. The charge of micro-particles in a low pressure spatial plasma afterglow. *J. Phys. Appl. Phys.* **2019**, *52*, 32LT03. [CrossRef]
30. Van Minderhout, B.; Van Huijstee, J.C.A.; Platier, B.; Peijnenburg, T.; Blom, P.; Kroesen, G.M.W.; Beckers, J. Charge control of micro-particles in a shielded plasma afterglow. *Plasma Sources Sci. Technol.* **2020**, *29*, 11. [CrossRef]
31. Staps, T.J.A.; Donders, T.J.M.; Platier, B.; Beckers, J. In-situ measurement of dust charge density in nanodusty plasma. *J. Phys. D Appl. Phys.* **2021**, *55*, 08LT01. [CrossRef]
32. Van De Wetering, F.M.; Brooimans, R.J.; Nijdam, S.; Beckers, J.; Kroesen, G.M. Fast and interrupted expansion in cyclic void growth in dusty plasma. *J. Phys. D Appl. Phys.* **2015**, *48*, 035204. [CrossRef]
33. Beckers, J.; Stoffels, W.W.; Kroesen, G.M. Temperature dependence of nucleation and growth of nanoparticles in low pressure Ar/CH4 RF discharges. *J. Phys. D Appl. Phys.* **2009**, *42*, 155206. [CrossRef]
34. Berndt, J.; Hong, S.; Kovačević, E.; Stefanović, I.; Winter, J. Dust particle formation in low pressure Ar/CH4 and Ar/C2H2 discharges used for thin film deposition. *Vacuum* **2003**, *71*, 377–390. [CrossRef]
35. Bouchoule, A.; Boufendi, L. Particulate formation and dusty plasma behaviour in argon-silane RF discharge. *Plasma Sources Sci. Technol.* **1993**, *2*, 204. [CrossRef]
36. Donders, T.; Staps, T.; Beckers, J. Characterization of cyclic dust growth in a low-pressure, radio-frequency driven argon-hexamethyldisiloxane plasma. *J. Phys. D Appl. Phys.* **2022**, *55*, 395203. [CrossRef]
37. Despax, B.; Makasheva, K.; Caquineau, H. Cyclic powder formation during pulsed injection of hexamethyldisiloxane in an axially asymmetric radiofrequency argon discharge. *J. Appl. Phys.* **2012**, *112*. [CrossRef]
38. Bouchoule, A. *Dusty Plasmas: Physics, Chemistry and Technological Impacts in Plasma Processing*; Wiley: Hoboken, NJ, USA, 1999; p. 408.
39. Fridman, A.A.; Boufendi, L.; Hbid, T.; Potapkin, B.V.; Bouchoule, A. Dusty plasma formation: Physics and critical phenomena. Theoretical approach. *J. Appl. Phys.* **1998**, *79*, 1303. [CrossRef]
40. Nunomura, S.; Shiratani, M.; Koga, K.; Kondo, M.; Watanabe, Y. Nanoparticle coagulation in fractionally charged and charge fluctuating dusty plasmas. *Phys. Plasmas* **2008**, *15*, 080703. [CrossRef]
41. Herrebout, D.; Bogaerts, A.; Gijbels, R.; Goedheer, W.J.; Vanhulsel, A. A one-dimensional fluid model for an acetylene RF discharge: A study of the plasma chemistry. *IEEE Trans. Plasma Sci.* **2003**, *31*, 659–664. [CrossRef]
42. Stoykov, S.; Eggs, C.; Kortshagen, U. Plasma chemistry and growth of nanosized particles in a C2H2 RF discharge. *J. Phys. D Appl. Phys.* **2001**, *34*, 2160. [CrossRef]

43. Mao, M.; Benedikt, J.; Consoli, A.; Bogaerts, A. New pathways for nanoparticle formation in acetylene dusty plasmas. *J. Phys. D Appl. Phys.* **2008**, *41*, 225201. [CrossRef]
44. Jiménez, M.; Tanarro, I.; Herrero, V.J. Time evolution of neutral and charged species in Ar/C2H2 capacitively-coupled RF discharges. *Plasma Sources Sci. Technol.* **2022**, *31*, 065003. [CrossRef]
45. Kortshagen, U.R.; Bhandarkar, U.V.; Swihart, M.T.; Girshick, S.L. Generation and growth of nanoparticles in low-pressure plasmas. *Pure Appl. Chem.* **1999**, *71*, 1871–1877. [CrossRef]
46. Warthesen, S.J.; Girshick, S.L. Numerical simulation of the spatiotemporal evolution of a nanoparticle-plasma system. *Plasma Chem. Plasma Process.* **2007**, *27*, 292–310. [CrossRef]
47. Agarwal, P.; Girshick, S.L. Sectional modeling of nanoparticle size and charge distributions in dusty plasmas. *Plasma Sources Sci. Technol.* **2012**, *21*, 055023. [CrossRef]
48. De Bleecker, K.; Bogaerts, A.; Goedheer, W. Modelling of nanoparticle coagulation and transport dynamics in dusty silane discharges. *N. J. Phys.* **2006**, *8*, 178. [CrossRef]
49. Greiner, F.; Melzer, A.; Tadsen, B.; Groth, S.; Killer, C.; Kirchschlager, F.; Wieben, F.; Pilch, I.; Krüger, H.; Block, D.; et al. Diagnostics and characterization of nanodust and nanodusty plasmas. *Eur. Phys. J. D* **2018**, *72*, 81. [CrossRef]
50. Groth, S.; Greiner, F.; Tadsen, B.; Piel, A. Kinetic Mie ellipsometry to determine the time-resolved particle growth in nanodusty plasmas. *J. Phys. D Appl. Phys.* **2015**, *48*, 465203. [CrossRef]
51. Groth, S.; Greiner, F.; Piel, A. Spatio-temporally resolved investigations of layered particle growth in a reactive argon-acetylene plasma. *Plasma Sources Sci. Technol.* **2019**, *28*, 115016. [CrossRef]
52. Asnaz, O.H.; Jung, H.; Greiner, F.; Piel, A. Size and density evolution of a single microparticle embedded in a plasma. *Phys. Plasmas* **2017**, *24*, 83701. [CrossRef]
53. Schepers, L.; Beckers, J.; IJzerman, W. Determination of microparticle characteristics in an etching plasma. *Contrib. Plasma Phys.* **2018**, *58*, 985–994. [CrossRef]
54. Kohlmann, N.; Wieben, F.; Han Asnaz, O.; Block, D.; Greiner, F. High-precision in-situ size measurements of single microparticles in an RF plasma. *Phys. Plasmas* **2019**, *26*, 53701. [CrossRef]
55. Onofri, F.R.; Wozniak, M.; Barbosa, S. On the Optical Characterisation of Nanoparticle and their Aggregates in Plasma Systems. *Contrib. Plasma Phys.* **2011**, *51*, 228–236. [CrossRef]
56. Barbosa, S.; Onofri, F.R.; Couëdel, L.; Wozniak, M.; Montet, C.; Pelcé, C.; Arnas, C.; Boufendi, L.; Kovacevic, E.; Berndt, J.; et al. An introduction to light extinction spectrometry as a diagnostic for dust particle characterisation in dusty plasmas. *J. Plasma Phys.* **2016**, *82*, 1–24. [CrossRef]
57. Eom, G.S.; Park, C.W.; Shin, Y.H.; Chung, K.H.; Park, S.; Choe, W.; Hahn, J.W. Size determination of nanoparticles in low-pressure plasma with laser-induced incandescence technique. *Appl. Phys. Lett.* **2003**, *83*, 1261–1263. [CrossRef]
58. Daun, K.J.; Stagg, B.J.; Liu, F.; Smallwood, G.J.; Snelling, D.R. Determining aerosol particle size distributions using time-resolved laser-induced incandescence. *Appl. Phys. B Lasers Opt.* **2007**, *87*, 363–372. [CrossRef]
59. Sipkens, T.A.; Mansmann, R.; Daun, K.J.; Petermann, N.; Titantah, J.T.; Karttunen, M.; Wiggers, H.; Dreier, T.; Schulz, C. In situ nanoparticle size measurements of gas-borne silicon nanoparticles by time-resolved laser-induced incandescence. *Appl. Phys. B Lasers Opt.* **2014**, *116*, 623–636. [CrossRef]
60. Yatom, S.; Bak, J.; Khrabryi, A.; Raitses, Y. Detection of nanoparticles in carbon arc discharge with laser-induced incandescence. *Carbon* **2017**, *117*, 154–162. [CrossRef]
61. Van De Wetering, F.M.; Oosterbeek, W.; Beckers, J.; Nijdam, S.; Kovačević, E.; Berndt, J. Laser-induced incandescence applied to dusty plasmas. *J. Phys. D Appl. Phys.* **2016**, *49*, 295206. [CrossRef]
62. Boufendi, L.; Hermann, J.; Bouchoule, A.; Dubreuil, B.; Stoffels, E.; Stoffels, W.W.; De Giorgi, M.L. Study of initial dust formation in an ArSiH4 discharge by laser induced particle explosive evaporation. *J. Appl. Phys.* **1994**, *76*, 148. [CrossRef]
63. Smirnov, R.D.; West, W.P.; Krasheninnikov, S.I.; Pigarov, A.Y.; Rosenberg, M.; Bray, B.D. Laser-dust interaction and dust size distribution measurements on DIII-D. *Phys. Plasmas* **2007**, *14*, 112507. [CrossRef]
64. Platier, B.; Staps, T.J.; Van Der Schans, M.; Ijzerman, W.L.; Beckers, J. Resonant microwaves probing the spatial afterglow of an RF plasma jet. *Appl. Phys. Lett.* **2019**, *115*, 254103. [CrossRef]
65. Van Ninhuijs, M.A.; Daamen, K.A.; Franssen, J.G.; Conway, J.; Platier, B.; Beckers, J.; Luiten, O.J. Microwave cavity resonance spectroscopy of ultracold plasmas. *Phys. Rev. A* **2019**, *100*, 061801. [CrossRef]
66. van der Schans, M.; Platier, B.; Koelman, P.; de Wetering, F.v.; Van Dijk, J.; Beckers, J.; Nijdam, S.; IJzerman, W. Decay of the electron density and the electron collision frequency between successive discharges of a pulsed plasma jet in N2. *Plasma Sources Sci. Technol.* **2019**, *28*, 035020. [CrossRef]
67. Pozar, D.M. *Microwave Engineering*, 3rd ed.; John Wiley & Sons: Hoboken, NJ, USA, 2011.
68. Mott-Smith, H.M.; Langmuir, I. The Theory of Collectors in Gaseous Discharges. *Phys. Rev.* **1926**, *28*, 727. [CrossRef]
69. Schweigert, I.V.; Alexandrov, A.L.; Ariskin, D.A. Effect of nanoparticles on discharge plasma and first steps of their formation. *Plasma Chem. Plasma Process.* **2014**, *34*, 671–702. [CrossRef]
70. Bhandarkar, U.V.; Swihart, M.T.; Girshick, S.L.; Kortshagen, U.R. Modelling of silicon hydride clustering in a low-pressure silane plasma. *J. Phys. D Appl. Phys.* **2000**, *33*, 2731. [CrossRef]
71. De Bleecker, K.; Bogaerts, A.; Goedheer, W. Detailed modeling of hydrocarbon nanoparticle nucleation in acetylene discharges. *Phys. Rev.-Stat. Nonlinear Soft Matter Phys.* **2006**, *73*, 026405. [CrossRef]

72. Trunec, D.; Zajíčková, L.; Buršíková, V.; Studnička, F.; Sťahel, P.; Prysiazhnyi, V.; Peřiná, V.; Houdkov, J.; Navártil, Z.; Franta, D. Deposition of hard thin films from HMDSO in atmospheric pressure dielectric barrier discharge. *J. Phys. D Appl. Phys.* **2010**, *43*, 225403. [CrossRef]
73. Dworschak, M.; Asnaz, O.H.; Greiner, F. A minimally invasive electrostatic particle extractor for nanodusty plasmas and its application for the verification of in situ Mie polarimetry. *Plasma Sources Sci. Technol.* **2021**, *30*, 035011. [CrossRef]
74. Killer, C.; Mulsow, M.; Melzer, A. Spatio-temporal evolution of the dust particle size distribution in dusty argon rf plasmas. *Plasma Sources Sci. Technol.* **2015**, *24*, 025029. [CrossRef]
75. Chutia, B.; Deka, T.; Bailung, Y. A nanodusty plasma experiment to create extended dust clouds using reactive argon acetylene plasmas . *Phys. Plasmas* **2021**, *28*, 63703. [CrossRef]
76. Mitic, S.; Pustylnik, M.Y.; Morfill, G.E.; Kovačević, E. In situ characterization of nanoparticles during growth by means of white light scattering. *Opt. Lett.* **2011**, *36*, 3699. [CrossRef]